

¹DRAFT VERSION NOVEMBER 26, 2019
 Typeset using L^AT_EX preprint style in AASTeX62

The circumstellar environment around the embedded protostar EC 53

SEOKHO LEE,¹ JEONG-EUN LEE,¹ YURI AIKAWA,² GREGORY HERCZEG,³ AND DOUG JOHNSTONE^{4,5}

¹*School of Space Research, Kyung Hee University, 1732 Deogyeong-daero, Giheung-gu, Yongin-si, Gyeonggi-do, Korea;*
jeongeunlee@khu.ac.kr

²*Department of Astronomy, University of Tokyo, 7-3-1 Hongo, Bunkyo-ku, Tokyo 113-0033, Japan*

³*Kavli Institute for Astronomy and Astrophysics, Peking University, Yi He Yuan Lu 5, Haidian Qu, 100871, Beijing, PR China*

⁴*NRC Herzberg Astronomy and Astrophysics, 5071 West Saanich Rd, Victoria, BC, V9E 2E7, Canada*

⁵*Department of Physics and Astronomy, University of Victoria, Victoria, BC, V8P 1A1, Canada*

ABSTRACT

EC53 is an embedded protostar with quasi-periodic emission in the near-IR and sub-mm. We use ALMA high-resolution observations of continuum and molecular line emission to describe the circumstellar environment of EC 53. The continuum image reveals a disk with a flux that suggests a mass of $0.075 M_{\odot}$, much less than the estimated mass in the envelope, and an in-band spectral index that indicates grain growth to centimeter sizes. Molecular lines trace the outflow cavity walls, infalling and rotating envelope, and/or the Keplerian disk. The rotation profile of the C¹⁷O 3–2 line emission cannot isolate the Keplerian motion clearly although the lower limit of the protostellar mass can be calculated as $0.3 \pm 0.1 M_{\odot}$ if the Keplerian motion is adopted. The weak CH₃OH emission, which is anti-correlated with the H¹³CO⁺ 4–3 line emission, indicates that the water snow line is more extended than what expected from the current luminosity, attesting to bygone outburst events. The extended snow line may persist for longer at the disk surface because the lower density increases the freeze-out timescale of methanol and water.

Keywords: protoplanetary disk, astrochemistry, numerical

1. INTRODUCTION

Low mass protostars form through the gravitational collapse of molecular cloud cores. The core material accretes onto protostars through a temporal reservoir, the accretion disk. Historical star formation models with a constant accretion rate of a few $10^{-6} M_{\odot} \text{yr}^{-1}$ (e.g., Shu 1977; Masunaga & Inutsuka 2000) predict protostellar luminosities that are much higher than the actual luminosities of most protostars (e.g., Kenyon et al. 1990; Enoch et al. 2009; Dunham et al. 2010). One promising solution of this luminosity problem is the episodic accretion, although other time-dependent solutions are also possible (see the discussion of Hartmann et al. (2016) and Fischer et al. (2017)).

Several observational phenomena support the episodic accretion directly or indirectly. Bursts in the optical brightness with various time scales are observed in FU Orionis objects (e.g., Herbig 1977, 2008; Audard et al. 2014) and EXors (e.g., Aspin & Reipurth 2000; Kospal et al. 2008; Lorenzetti et al. 2012).

¹ Seokho Lee moved to National Astronomical Observatory of Japan (seokho.lee@nao.ac.jp).

Knots along jets and clumpy structures in protostellar outflows (e.g., Plunkett et al. 2015) could be also induced by accretion variability. In addition, the variation in accretion luminosity affects the chemistry in the disk and envelope (e.g., Lee 2007; Visser et al. 2015); the $15.2\ \mu\text{m}$ pure CO₂ ice absorption features toward low-luminosity protostars (Kim et al. 2012) and the extended snow lines of volatiles compared to the theoretical snow line locations expected from the current luminosity (Jørgensen et al. 2013, 2015) are explained by past bursts of accretion. Brightness variation in the sub-mm by the accretion burst is detectable even for embedded protostars (Johnstone et al. 2013), as demonstrated for the Class 0 star HOPS 383 and two massive protostars (Safron et al. 2015; Hunter et al. 2017; Liu et al. 2018).

Although the mechanism of episodic accretion in protostars has not yet been securely identified, two main ideas are proposed to explain the large accretion bursts. First, disk instabilities, such as thermal instability (Bell & Lin 1994), gravitational instability (e.g., Vorobyov & Basu 2010), and the combined effect of both magnetorotational instability and gravitational instability (Zhu et al. 2009; Bae et al. 2014), may trigger a large amount of mass to accrete through the disk and onto the star. The other type of possible mechanism is the perturbation of the disk by an external trigger, such as a binary companion (Bonnell & Bastien 1992), the tidal disruption of radially migrating gas clumps/giant planets (Vorobyov & Basu 2005; Nayakshin & Lodato 2012), or disk variability linked to a stellar magnetic cycle (Armitage 1995; D’Angelo & Spruit 2012; Armitage 2016). The role of these mechanisms may be more important at earlier stages in protostellar growth, however any evolutionary change is difficult to evaluate with most surveys, since the common optical and near-IR survey probe later stages in the evolution of young stellar objects (e.g. Hillenbrand & Findeisen 2015; Contreras et al. 2017, 2019).

Recently, the JCMT-Transient monitoring survey has been searching for variability at the protostellar stage with monthly monitoring of sub-mm continuum emission in eight nearby star-forming regions (Herczeg et al. 2017). The first sub-mm variable detected in this survey, EC 53 (Yoo et al. 2017), stands out in amplitude relative to other protostars in the 8 fields (Mairs et al. 2017; Johnstone et al. 2018). EC 53, first identified by Eiroa & Casali (1992) as a member of the Serpens Main Cloud (distance of 436 ± 9 pc Ortiz-León et al. 2017), is an embedded protostar with a bolometric luminosity of $1.7 - 4.8\ L_\odot$ (Evans et al. 2009; Enoch et al. 2009; Gutermuth et al. 2009; Dionatos et al. 2010; Dunham et al. 2015). Past near-IR monitoring shows that the K magnitude of EC 53 varies with a period of ~ 543 days (Hodapp 1999; Hodapp et al. 2012). The sub-mm observations (Yoo et al. 2017) confirm this periodicity and strongly suggests that this sub-mm variability should be induced by the variable accretion rate. In addition, this short ~ 1.5 years variability may be related with a very close companion or a protoplanet, which can induce the periodic gravitational instability in the disk (Lodato & Clarke 2004). This short-period brightness variation of an embedded protostar in sub-mm casts an important question on when planets start to form.

The range of instabilities and the consequences of outbursts are both expected to leave traces in the circumstellar environment in the immediate vicinity of the protostar. To better describe the kinematics and chemical properties of this environment, we have obtained high-resolution Atacama Large Millimeter/submillimeter Array (ALMA) imaging of gas and dust.

2. OBSERVATIONS

The observation of EC 53 was carried out with ALMA during Cycle 4 (2016.1.01304.T, PI: Jeong-Eun Lee) on 2017 May 21. The four spectral windows were set for $336.995 - 337.229\ \text{GHz}$, $338.345 - 338.579\ \text{GHz}$, $346.945 - 347.180\ \text{GHz}$, and $349.396 - 349.630\ \text{GHz}$, each with a spectral resolution of $244.141\ \text{kHz}$ ($\sim 0.2\ \text{km s}^{-1}$). This setup contains C¹⁷O 3–2, CH₃OH 7_k – 6_k, H¹³CO⁺ 4–3, CCH N= 4–3, J= 7/2–5/2,

F= 4–3 and F= 3–2 lines. Forty-one 12-m antennas were used in the C40-5 configuration, with baselines in the range from 15.1 m to 1.1 km. The total observing time on EC 53 was 48.1 minutes.

The data were initially calibrated using the CASA 4.7.2 pipeline (McMullin et al. 2007). The quasar J1751+0939 was used as a bandpass and amplitude calibrator, and the nearby quasar J1830+0619 was used as a phase calibrator. Self-calibration was applied for better imaging.

For molecular lines, natural weighting with a UV-taper of 0.2'' was used to obtain images with a higher signal-to-noise ratio and a resolution of 0.3''. A spectral resolution of 0.25 km s⁻¹ was used for *strong* C¹⁷O, H¹³CO⁺, and CCH lines, while 0.5 km s⁻¹ was used for *weak* lines to reduce the RMS noise (Table 1). The RMS noise level for the strong molecular lines is \sim 4 mJy beam⁻¹ near the continuum peak. The images of C¹⁷O, H¹³CO⁺, and two strong CCH lines were produced by Briggs weighting with a robust factor of 0.5 to obtain higher resolution (0.2'').

A dust continuum image was produced using line-free channels and was cleaned with two weightings: (1) natural weighting with the UV-taper of 0.2'' to compare with the molecular line images and (2) uniform weighting only with the UV distances longer than 500 k λ to obtain a higher spatial resolution, with a beam size of 0.15'' \times 0.11'' oriented at position angle of -88.4°. The RMS noise levels of the two images are 0.21 and 0.38 mJy beam⁻¹, respectively. The data are analyzed in the image plane.

3. RESULTS

3.1. *Dust continuum images*

The 343.4 GHz (873 μ m) continuum image with a lower resolution (Figure 1) shows extended emission along the north-south direction as well as a compact source. The compact source is resolved in the higher resolution image as shown on the left panel of Figure 2. The compact emission could originate from the disk (see Sections 3.2.1 and 4.1). The properties of the continuum emission are derived by fitting a Gaussian profile using the task ‘imfit’ in CASA.

The peak of the continuum emission is located at α (J2000)= 18^h29^m51.17685^s and δ (J2000)= +01^d16^m40.3892''. This peak position is consistent to within \sim 0.2'' of the positions from *Spitzer* (Harvey et al. 2006; Hsieh & Lai 2013), VLA (Ortiz-León et al. 2015), and high-resolution Keck K_S -band imaging (Hodapp et al. 2012), after applying the proper motion correction for Serpens Main of \sim 10 mas yr⁻¹ towards the south-east (Ortiz-León et al. 2017; Herczeg et al. 2019). The position is offset to the north of the 2MASS (Cutri et al. 2003) and neoWISE (Cutri & et al. 2014) positions, likely a result of nebulosity seen to the south of the EC 53 binary system by Hodapp et al. (2012).

The deconvolved image of the disk shows that the major and minor axes are 144.2 ± 2.4 mas and 118.4 ± 2.2 mas with a position angle of 60.0 ± 4.2 °. The ratio of the major and minor axes suggests the disk inclination of 34.8 ± 2.1 °. When this position angle and the inclination are adopted, the disk radius that encircles 95% of the disk flux is 214 mas (93 AU at the distance of 436 pc), similar to the typical size of more evolved protoplanetary disks (e.g. Tripathi et al. 2017; Cieza et al. 2019; Long et al. 2019).

This position angle and inclination are both consistent with previous observations. The observed position angle of the disk is roughly perpendicular to the direction of the H₂ jet at 140° (Herbst et al. 1997) and the ¹²CO 3–2 outflow at 135° (Dionatos et al. 2010). Hodapp et al. (2012) suggested that the disk of EC 53 is seen nearly edge-on based on the cometary feature in the near-IR image. However, the inclination of the outflow axis could be lower than the half-opening angle of the outflow cavity when a protostar is observed in near-IR scattered light (Reipurth et al. 2000). Indeed, the near-IR image of EC 53 (Figure 6 in Hodapp et al. 2012, see the blue dashed curve on the bottom right panel in Figure 3) indicates that the half-opening

angle of the outflow cavity is smaller than 45° and the inclination is between 30° and 45° (see Figure 17 in [Reipurth et al. 2000](#)). The best-fit spectral energy distribution model of EC 53 also **requires** a small inclination of 30° (Baek et al. submitted). Furthermore, for Class I sources, [Fe II] forbidden lines trace high velocity gas with a radial velocity of $100 - 200 \text{ km s}^{-1}$ ([Davis et al. 2011](#)). Near-IR spectra of EC 53 show that the $1.644 \mu\text{m}$ [Fe II] line is blue-shifted by $\sim 170 \text{ km s}^{-1}$ (S. Park et al. in prep), which implies that the inclination of the jet should be close to face-on.

The peak intensity and total flux of the disk, which are measuring by applying ‘imfit’ to the left image of Figure 2, are $69.3 \pm 0.4 \text{ mJy beam}^{-1}$ and $139.7 \pm 1.2 \text{ mJy}$, respectively. The compact emission shown in the lower resolution image (Figure 1) has the flux of 155 mJy within an aperture of $0.7''$, implying that the compact emission is mostly radiated from the disk shown in the high resolution image (Figure 2). On the other hand, the total continuum flux in Figure 1 is 330 mJy . The $850 \mu\text{m}$ flux (in the beam of $14.6''$) of EC 53 with the JCMT/SCUBA-2 is 960 mJy at the quiescent phase ([Yoo et al. 2017](#)), and thus, at least 60% of the continuum emission arises from an extended envelope and is resolved out in this ALMA observation.

The disk mass may be estimated from the continuum flux by

$$M_{\text{disk}} = \frac{F_\nu d^2}{\kappa_\nu B_\nu(T_{\text{dust}})}, \quad (1)$$

where F_ν is the observed flux ($139.7 \pm 1.2 \text{ mJy}$), d is the distance to EC 53, κ_ν is the dust opacity, and $B_\nu(T_{\text{dust}})$ is the Planck function with the dust temperature of T_{dust} . Adopting an average dust temperature of 20 K (following [Andrews 2005](#)), a dust opacity $\kappa_\nu = 3.4 \text{ cm}^2 \text{ g}^{-1}$ ([Beckwith et al. 1990](#)), and a gas-to-dust ratio of 100 leads to a disk mass of $0.075 \pm 0.003 \text{ M}_\odot$. This estimate for disk mass is consistent with standard techniques but depends on highly uncertain assumptions, including the dust opacities and optical depths (see review by [Williams & Cieza 2011](#)).

The right panel of Figure 2 shows the spectral index α between two continuum images produced with the uniform weighting at frequencies of $\nu_1 = 348.38 \text{ GHz}$ and $\nu_2 = 337.86 \text{ GHz}$. The spectral index has a relation with the optical depth $\tau_{343.4\text{GHz}}$ and the power-law index of the dust opacity β as

$$\frac{F_{\nu_1}}{F_{\nu_2}} = \left(\frac{\nu_1}{\nu_2} \right)^\alpha = \frac{B_{\nu_1}(T)(1 - \exp(-\tau_{\nu_1}))}{B_{\nu_2}(T)(1 - \exp(-\tau_{\nu_2}))}, \quad (2)$$

$$\tau_{\nu_i} = \tau_{343.4\text{GHz}} \left(\frac{\nu_i}{343.4\text{GHz}} \right)^\beta, \quad (3)$$

where F_{ν_i} and τ_{ν_i} are the flux and optical depth at the frequency ν_i . The spectral index at the continuum peak is 1.9 ± 0.3 , which implies that either the disk is optically thick at 343.4 GHz and/or that dust grains have grown (see Section 4.1).

The JCMT/SCUBA-2 $850 \mu\text{m}$ flux of EC 53 after removing the contribution of the disk implies the envelope mass is $0.86 - 1.25 \text{ M}_\odot$ (see Equation (1) in [Jørgensen et al. 2009](#)). The disk to envelope mass ratio, 6 – 9%, implies that EC 53 could be a late Class 0 (1 - 10%) or an early Class I source (20 – 60 %) ([Jørgensen et al. 2009](#)). This is consistent with the early Class I stage ([Dunham et al. 2015](#)) derived from the bolometric temperature ($T_{\text{bol}} = 130 \text{ K}$) of the SED, although a continuum radiative transfer model is needed to estimate more accurate disk and envelope masses.

3.2. Molecular lines

In this section, we infer the morphology of the circumstellar material by measuring gas kinematics in the spectral images of emission lines. The different emission lines probe the disk, infall, and outflows of the source, as described below. A source velocity of 8.5 km s^{-1} is adopted throughout this analysis, based on the rotation profile of the C^{17}O line along the disk direction (Section 3.2.1). This value is similar to a previous measurement of $\sim 8.35 \text{ km s}^{-1}$ using N_2H^+ 1–0 line emission measured with the CARMA (Combined Array for Research in Millimeter-wave Astronomy) data that has a beam size of $7''$ (Lee et al. 2014), with a slight offset that may be explained because the N_2H^+ species is depleted at the source position (Figure 4).

Figure 3 shows integrated intensity maps for the detected molecular lines toward EC 53. H^{13}CO^+ 4–3, C^{17}O 3–2, and CCH N= 4–3, J= 7/2–5/2, F= 4–3, F= 3–2 (in the bottom panels) consist of compact emission near the continuum peak and more extended emission while C^{34}S 8–7, CH_3OH , and other weak CCH lines (in the top panels) show only compact and weak emission near the continuum source. Those weak CH_3OH and CCH lines are stacked individually to get a higher signal-to-noise ratio. The observed lines are listed in Table 1.

The integrated intensity maps of the H^{13}CO^+ and C^{17}O lines generally show similar distributions. Both lines have red-shifted and blue-shifted components in the north and south, respectively, as shown in the intensity weighted velocity map (Figure 5). The velocity channel maps of C^{17}O and H^{13}CO^+ (Figures 6 and 7) show that the red-shifted components ($9.00 - 9.75 \text{ km s}^{-1}$) have decreasing velocity with the distance from the protostar. Such a profile is expected for red-shifted emission from infalling (accreting) material, as also seen in the Class I source L1489 IRS (Yen et al. 2014). The same trend is also observed in the C^{17}O blue-shifted components ($8.00 - 7.25 \text{ km s}^{-1}$) near the protostar ($r < 1''$). On the other hand, the blue-shifted velocity ($8.50 - 7.75 \text{ km s}^{-1}$) increases with the distance from the protostar at $r \geq 1''$. This implies that the blue-shifted emission at the scale of $r \geq 1''$ traces the gas in the outflow cavity wall (e.g., Arce et al. 2013). The blue-shifted monopolar outflow could be due to an asymmetric structure of the circumstellar environment (Loinard et al. 2013).

At the continuum peak, absorption against the continuum emission is detected in the H^{13}CO^+ and strong CCH lines, while self-absorption is detected in the C^{17}O line (Figure 8). This deep absorption below the continuum level in the H^{13}CO^+ and strong CCH lines is red-shifted, tracing the infalling envelope material (Evans et al. 2015). The high velocity ($|\Delta V| > 1 \text{ km s}^{-1}$ from the source velocity) emission feature detected in the C^{17}O line (the red spectrum in Figure 8), which may trace the disk rotation, is missing in the H^{13}CO^+ line. Figure 7 shows that there is no H^{13}CO^+ line emission within $\sim 0.2''$ from the protostar. The related chemistry for this phenomenon is discussed in Section 4.2.

The strong CCH line emission (the bottom right contour image of Figure 3) seems to trace the outflow cavity walls. The stream to the east, which appears distributed along the blue-shifted outflow cavity wall, is also seen in the near-IR narrow band image covering the H_2 emission (Hodapp et al. 2012). Another stream toward the north direction looks like a mirror image of the eastward stream with respect to the disk midplane (the solid gray line in Figure 3), which could imply that the northward stream might trace the red-shifted outflow cavity wall. CCH emission along the outflow cavity walls is also found in L1527, IRAS 15398-3359, and L483 (Oya et al. 2014; Sakai et al. 2014; Oya et al. 2017).

The CH_3OH and other weak CCH lines are marginally detected (see Table 1). While the CH_3OH lines are detected near the continuum peak, the weak CCH lines are missing toward the continuum source, instead peaking at $0.55''$ from the continuum peak along the disk direction. The same phenomenon has been observed in other sources: in L1527, IRAS 15398-3359, and L483 the CCH is also depleted near the con-

tinuum peak and has strong emission off the peak (Oya et al. 2014; Sakai et al. 2014; Oya et al. 2017). The CCH molecule reacts with H₂ at warm temperatures (see e.g., Aikawa et al. 2012) and could be destroyed by those gas phase reaction in the warm and dense inner envelope and/or frozen on the dust grain in the cold and dense disk.

The C³⁴S 8–7 line seems to trace the dense molecular gas near the continuum peak as well as in the outflow cavity wall. The SiO 7–6 line was also observed but not detected.

3.2.1. Kinematics of C¹⁷O 3–2: Disk vs. Infalling rotating envelope?

The rotation profile along the disk direction provides evidence of the kinematics of the disk. Figure 9 shows velocity channel maps for C¹⁷O near the continuum peak. The innermost regions have a position-velocity distribution that would be expected for a disk. Beyond 0.5'' along the position angle of 60° (the black solid line in Figure 9), the spatial distribution of red-shifted components (9.75 and 9.50 km s⁻¹) implies that this emission might not be associated with the disk. In the following analysis, we fit the rotation profile only within 0.5''. The highest velocity components are close to the protostar, and the models with different position angles from 30° to 60° do not show significant variation in the rotation profile.

Figure 10 shows the position-velocity diagram along the disk (left) and the rotation velocity profiles (right) of EC 53. The power-law index that fits the velocity profile is -2.1 ± 2.2 . If the highest blue-shifted point is excluded, the best-fit power law is -1.1 ± 0.7 , indicative of the rotating infalling envelope under the constraint of angular momentum conservation (Sakai et al. 2014). However, our current observation with large scatter and a low signal-to-noise ratio cannot rule out a rotational profile produced by the Keplerian disk. The range of the rotation velocity corresponds to the Keplerian motions with the protostellar masses of 0.2 and 0.4 M_⊙ when we adopted the inclination of 35°. Since the protostar is still young and the envelope massive, the present-day protostellar mass may be much lower than the final mass after stellar assembly is complete.

4. DISCUSSION

4.1. Dust grain growth

The observed 873 μm continuum emission is mainly from dust thermal emission. In the continuum images produced with uniform weighting, the peak intensity and the spectral index at the continuum peak are 69.3 ± 0.4 mJy beam⁻¹ and 1.9 ± 0.3 , respectively. The spectral index lower than 2 cannot be explained by non-thermal emission, since VLA 4.5 and 7.5 GHz observations (with a beam size of $\sim 0.4''$, Ortiz-León et al. 2015) indicate that the 873 μm flux from the non-thermal emission is lower than 0.2 mJy. Therefore, the spectral index of 1.9 ± 0.3 implies that the continuum emission is optically thick and/or that the power-law index of dust opacity is lower than 1 in the isothermal condition.

The sub-mm continuum spectral index can be used to derive the properties of emitting sources and dust grains. The low spectral index (1.9 ± 0.3) for the dust continuum emission indicates that the compact continuum emission could be emitted from the disk. On the other hand, the spectral index derived from the ACA (Atacama Compact Array) images of EC 53 in band 6 and 7, which trace the envelope of EC 53, is about 2.5 (W. Park, in prep.). Continuum emission images at 1.1 mm and 3 mm toward two Class I sources Elias 29 and WL 12 show that the spectral indices in the disk are typically lower than 2, while in the envelope are typically higher than 2.5 (Miotello et al. 2014). Figure 11 shows the optical depth and the power-law index of dust opacity, β , for given dust temperatures reproducing the observed spectral index of 1.9 ± 0.3 . When we adopt the dust temperature of 20 K and $\beta = 1$, which are used for the calculation of the disk mass, the average optical depth of dust continuum is $1.8_{-1.0}^{+2.2}$ (see the blue circle in Figure 11). If

this optical depth is considered, the disk mass derived by Equation (1) is smaller than the actual value by a factor of two. On the other hand, if we know the dust temperature and the optical depth of dust continuum, then we can derive β , which constrains the dust properties; grain growth in the disk reduces the power-law index of dust opacity (e.g., [Natta et al. 2007](#)).

The optical depth of the dust continuum can be derived from a molecular line. As shown in the integrated intensity maps for the detected molecular lines (Figure 3), the emission peaks of all the molecular lines are off the continuum peak. Figure 12 shows the C^{17}O 3–2 intensity map integrated over the velocity from 1.0 to 1.5 km s^{-1} with respect to the source velocity. This integrated intensity map was produced using the uniform weighting to trace how the C^{17}O emission is distributed near the continuum peak, by excluding the contribution of the extended emission. The C^{17}O line emission is clearly depleted near the continuum peak and peaks around 0.13'' from the continuum peak. This phenomenon was also observed in TMC 1A ([Harsono et al. 2018](#)) and V883 Ori ([Lee et al. 2019](#)). A high optical depth and strong emission of the dust continuum can reduce the intensity of the molecular line emission; the observed line intensity is reduced by $\exp(-\tau_c)$ with the dust optical depth of τ_c ([Yen et al. 2016](#); [Lee et al. 2019](#)).

We adopt a simple thin disk with power-law distributions for the continuum optical depth $\tau_c(r)$ and the dust temperature $T_{\text{dust}}(r)$:

$$\tau_c(r) = \tau_{0.1} \left(\frac{r}{0.1''} \right)^{-\psi}, \quad (4)$$

$$T_{\text{dust}}(r) = T_{0.1} \sqrt{\frac{0.1''}{r}}, \quad (5)$$

where $\tau_{0.1}$ and $T_{0.1}$ are the continuum optical depth and dust temperature at 0.1''. We test three power-law indices of optical depth: $\psi = 1.0, 1.5$, and 2.0 . The solid lines in Figure 13 indicate the models producing the observed 873 μm intensity at the continuum peak ($69.3 \pm 0.4 \text{ mJy beam}^{-1}$). The emission from the inclined thin disk (inclination= 35°) are convolved with the observed beam.

The C^{17}O intensity within 0.5'' (Figure 9) is lower than 45 mJy beam $^{-1}$, which corresponds to a brightness temperature (T_b) of ~ 14 K. If the gas and dust have the same temperature, the C^{17}O brightness temperature is about two times lower than the gas temperature, indicating that the C^{17}O line is optically thin. When we assume that the column density ratio of C^{17}O and dust is spatially constant, and the C^{17}O molecules are in the local thermal equilibrium (LTE) condition, the above thin disk model produces the C^{17}O emission distribution $I(r)$:

$$I(r) \propto \tau_c(r) \cdot n_u(T_{\text{dust}}(r)) \cdot \exp(-\tau_c(r)), \quad (6)$$

where the upper level population $n_u(r)$ is derived from the Boltzmann distribution with $T_{\text{dust}}(r)$. In the right hand side of Equation (6), the first term ($\tau_c(r)$) represents the total column density of C^{17}O , the second term ($n_u(T_{\text{dust}}(r))$) is the fraction of C^{17}O to produce the C^{17}O 3–2 line, and the third term indicates the extinction of the line by dust grains.

Our models with the dust temperature of 50 – 55 K and dust optical depth of 1.1 – 1.6 at the radius of 0.1'' can reproduce the C^{17}O emission peak around 0.13'' (see the circles in Figure 13 and Table 2). The thin dust disk with a truncated radius of 0.13'' can reproduce the observed continuum flux of 139.7 mJy as well as the disk size measured with ‘imfit’. The entire dust disk is optically thick, and thus, the C^{17}O emission peaks at the dust disk radius. When the dust opacity of $3.4 \text{ cm}^2 \text{ g}^{-1}$ at 343.4 GHz ([Beckwith et al. 1990](#)) and gas-to-dust ratio of 100 are adopted, the models show the disk mass is 0.1 M_\odot with an uncertainty by

a factor of two, which is similar to the disk mass of $0.075 M_{\odot}$ (see Section 3.1). Note that grain growth can change the dust opacity (e.g., Ricci et al. 2010), and thus, the disk mass. The calculated dust mass would also be 3.3 times lower if we use 50 K instead of 20 K for the average dust temperature in the disk.

For the dust temperature of ~ 50 K and the continuum optical depth of ~ 1.4 near the continuum peak in our model, the power-law index of the dust opacity (β) must be lower than 0.2 ± 0.6 to reproduce the observed spectral index of 1.9 ± 0.3 (see the black circle in Figure 11). This suggests that the maximum size of dust grains should be larger than centimeter sizes (e.g., Ricci et al. 2010; Testi et al. 2014). The large disk mass of about $0.1 M_{\odot}$ and the large grain size imply a possibility of planet formation even in the early evolutionary stage, as argued by Harsono et al. (2018).

4.2. Water and CO snowlines

Figure 14 shows the spectral maps of $H^{13}CO^+$ and $C^{17}O$ on top of the image of the CH_3OH integrated intensity map. Outside of the CH_3OH emission area, the $H^{13}CO^+$ line has a similar intensity to the $C^{17}O$ line. However, the $H^{13}CO^+$ line emission is depleted near the continuum peak, where the methanol lines emit. On the other hand, the $C^{17}O$ line is still strong and broad near the continuum peak where the $H^{13}CO^+$ emission completely disappears. The CH_3OH line might emit from the disk or infalling rotating inner envelope traced by $C^{17}O$ because the CH_3OH line has a similar line width to that of the $C^{17}O$ line. The emission peak of CH_3OH is offset from the continuum peak probably due to the optically thick continuum emission, as also shown in the $C^{17}O$ emission distribution. The anti-correlation between the $H^{13}CO^+$ and CH_3OH emission was also detected in IRAS 15398-3359 and may be caused by the destruction of $H^{13}CO^+$ by water, which evaporates simultaneously with CH_3OH (Jørgensen et al. 2013). The methanol emission is known to be related closely with water emission (Bjerkeli et al. 2016). However, the observed CH_3OH emission is extended up to $\sim 0.35''$ (see Figure 14), which is an order of magnitude larger than the water snow line expected from the current luminosity. In the thin disk model described above, the water snow line (100 K) is located around $0.03''$.

To measure the abundance of methanol, we first extracted the CH_3OH spectra with an aperture of $0.6''$. We then reproduced this spectrum with a simple LTE model using molecular data from the Cologne Database for Molecular Spectroscopy (CDMS, Müller et al. 2001). The model includes the dust continuum and opacity and assumes a line width of 2 km s^{-1} . The molecular hydrogen column density of $\sim 10^{25} \text{ cm}^{-2}$ is estimated from the dust continuum flux measured with the same $0.6''$ aperture when the dust opacity of $3.4 \text{ cm}^2 \text{ g}^{-1}$ (Beckwith et al. 1990), gas-to-dust ratio of 100, and the dust temperatures of 30, 50, and 70 K are adopted. The derived methanol column density and abundance are $\sim 10^{15} \text{ cm}^{-2}$ and $\sim 10^{-10}$, respectively (see Figure 15).

The methanol emission from the much larger outburst of V883 Ori provides a useful comparison for that from EC 53. The derived methanol abundance for EC 53 is two orders of magnitude lower than the CH_3OH abundance of $\sim 10^{-8}$ for V883 Ori (Lee et al. 2019) although the physical size of the methanol emission regions are similar for V883 Ori and EC 53. In both cases, the methanol abundance may be underestimated by an order of magnitude because of the optical depths of dust continuum and methanol itself (van 't Hoff et al. 2018; Lee et al. 2019).

The difference in abundance between EC 53 and V883 Ori, despite the similar size of methanol emission, might be related to the repeated outbursts and the 2-D structure of the sublimation region. The water/methanol sublimation occurs over the 2-D structure in the disk (van 't Hoff et al. 2018; Lee et al. 2019); the snow line extends to much larger radii at the disk surface than at the disk midplane. During the quiescent phase, the methanol freezes back onto grain surfaces very efficiently in the disk midplane but much more

slowly at the disk surface, where the density is much lower. As a result, if there were powerful burst events in the past in EC 53, the surface snow line could be very large, despite a much smaller snow line at the disk midplane because of the low current luminosity. This will make the derived abundance of gaseous CH_3OH low compared to the size of emission in EC 53. In contrast, V883 Ori has an ongoing outburst with the luminosity greater than that of EC 53 in the quiescent phase by two orders of magnitude. As a result, the snow line is large even at the disk midplane, resulting in the higher abundance of gaseous methanol in V883 Ori.

In summary, the different timescales for freeze-out between the disk midplane and surface may explain why the methanol emission region extends far beyond the location of the water snow line expected from the current luminosity of EC 53, despite the low overall abundance compared with V883 Ori. The repeated accretion bursts in EC 53 may extend the water snow line, and the disk surface will retain the larger snow line for a longer time than the disk midplane.

Grain growth in the disk midplane could also contribute to increasing the radius of the snow line in the disk midplane. When the ratio of scale height to radius is 0.1, the density at the midplane near $0.1''$ is $\sim 10^{11} \text{ cm}^{-3}$. If we adopt the typical ISM grain size ($0.1 \mu\text{m}$) and the typical abundance of the dust grain with respect to the molecular hydrogen ($\sim 10^{-12}$), then all methanol molecules freeze out onto the dust grain within a few days (Lee et al. 2004). However, the freeze-out timescale could be longer than a few years when the maximum grain size is larger than 1 cm (see Section 4.1), since the total surface area of grains would then be reduced by a factor of ~ 300 , assuming that the total grain mass is conserved, and the minimum size of grain and the power-law index of grain size distribution are $0.1 \mu\text{m}$ and -3.5, respectively. This freeze-out timescale is longer than the periodicity of 1.5 years in the accretion onto EC 53 (Yoo et al. 2017). The CH_3OH emission could trace the water snow line constructed during the burst phase of the period, when the luminosity is four times brighter (Yoo et al. 2017) and the water snow line would then be two times larger, or $\sim 0.06''$ (Min et al. 2011; Jørgensen et al. 2015; Visser et al. 2015). Although the CH_3OH emission could extend further than $0.06''$ at the disk surface because of the high temperature and low density in the irradiated disk (van 't Hoff et al. 2018; Lee et al. 2019), the measured size of the CH_3OH emission requires a more extreme (factor of ~ 100) luminosity enhancement.

Figure 4 shows that the N_2H^+ line emission is anti-correlated with the C^{17}O 3–2 line emission. It is hard to determine accurately the size of the N_2H^+ emission hole because of the low spatial resolution ($\sim 7''$) of CARMA. However, our C^{17}O ALMA data (Figures 3 and 6) indicate that the C^{17}O line extends to $\sim 2''$ along the disk midplane direction. In addition, in the ACA observation (Figure 4), the full width at half maximum of the C^{17}O 3–2 emission is about $2.7''$. This observed CO snow line ($\sim 1000 \text{ AU}$) is also larger than that expected from the luminosities both for the quiescent and burst phases ($\sim 250 \text{ AU}$ and $\sim 500 \text{ AU}$, respectively). These CO sublimation radii (25 K) are derived from the spectral energy distribution modelings of EC 53 (G. Baek et al. submitted.). Together, the estimated sizes of the C^{17}O emission and the N_2H^+ emission hole support suggestion of repeated and/or more extreme burst events in the past.

5. SUMMARY

We carried out high resolution ALMA observations toward EC 53. The main results are:

1) The continuum image at $873 \mu\text{m}$ shows that EC 53 has a massive disk ($0.075 \pm 0.003 \text{ M}_\odot$) with centimeter-size grains, implying that a planet could form even in the early evolutionary stage to induce the observed periodic variation of accretion rate. Furthermore, the optically thick dust continuum emission in the sub-mm reduces the molecular line emission near the continuum peak.

(2) The high velocity components of C^{17}O 3–2 show a rotation feature along the disk direction, however, the current observation cannot constrain whether the rotation profile is associated with the Keplerian disk and/or an infalling envelope. If the Keplerian motion is adopted, the rotation profile indicates that EC 53 has a protostellar mass of $\sim 0.3 \pm 0.1 \text{ M}_\odot$.

(3) The anti-correlation of CH_3OH and H^{13}CO^+ near the continuum peak could be associated with the destruction of H^{13}CO^+ by evaporated water molecules.

(4) The observed methanol and CO emissions are more extended than the snow lines expected due to the current luminosity, implying repeated and/or more extreme accretion burst events in the past. The luminosity and therefore the abundance of CH_3OH is two orders of magnitude lower than measured from disks undergoing larger outbursts, perhaps because the CH_3OH is frozen out at the disk midplane but is still in the gas phase in the lower-density disk surface.

This work was motivated and performed by the JCMT-Transient Team as part of a comprehensive effort to obtain and interpret time-domain sub-mm observations of star-forming regions. The authors appreciate the important contribution of the JCMT Transient Team members in observing, calibrating, and making available the JCMT sub-mm observations used for this paper. This work was supported by the Basic Science Research Program through the National Research Foundation of Korea (grant No. NRF-2018R1A2B6003423) and the Korea Astronomy and Space Science Institute under the R&D program supervised by the Ministry of Science, ICT and Future Planning. S. L. was also supported by NAOJ ALMA Scientific Research Grant Number of 2018-10B. Y.A. was supported by KAKENHI Grant Number 18H05222 and NAOJ ALMA Scientific Research Grant Number of 2019-13B. GJH is supported by general grant 11773002 awarded by the National Science Foundation of China. D.J. is supported by the National Research Council of Canada and by an NSERC Discovery Grant.

REFERENCES

Aikawa, Y., Wakelam, V., Hersant, F., Garrod, R. T., & Herbst, E. 2012, *ApJ*, 760, 40

Andrews, S. M. 2005, in *Protostars and Planets V Posters*, 8203

Arce, H. G., Mardones, D., Corder, S. A., et al. 2013, *ApJ*, 774, 39

Armitage, P. J. 1995, *MNRAS*, 274, 1242

—. 2016, *ApJL*, 833, L15

Aspin, C., & Reipurth, B. 2000, *MNRAS*, 311, 522

Audard, M., Ábrahám, P., Dunham, M. M., et al. 2014, *Protostars and Planets VI*, 387

Bae, J., Hartmann, L., Zhu, Z., & Nelson, R. P. 2014, *ApJ*, 795, 61

Beckwith, S. V. W., Sargent, A. I., Chini, R. S., & Guesten, R. 1990, *AJ*, 99, 924

Bell, K. R., & Lin, D. N. C. 1994, *ApJ*, 427, 987

Bjerkeli, P., Jørgensen, J. K., Bergin, E. A., et al. 2016, *A&A*, 595, A39

Bonnell, I., & Bastien, P. 1992, *ApJL*, 401, L31

Cieza, L. A., Ruíz-Rodríguez, D., Hales, A., et al. 2019, *MNRAS*, 482, 698

Contreras, Y., Rathborne, J. M., Guzman, A., et al. 2017, *MNRAS*, 466, 340

Contreras, Y., Rebolledo, D., Breen, S. L., Green, A. J., & Burton, M. G. 2019, *MNRAS*, 483, 1437

Cutri, R. M., & et al. 2014, *VizieR Online Data Catalog*, II/328

Cutri, R. M., Skrutskie, M. F., van Dyk, S., et al. 2003, *VizieR Online Data Catalog*, II/246

D’Angelo, C. R., & Spruit, H. C. 2012, *MNRAS*, 420, 416

Davis, C. J., Cervantes, B., Nisini, B., et al. 2011, *A&A*, 528, A3

Dionatos, O., Nisini, B., Codella, C., & Giannini, T. 2010, *A&A*, 523, A29

Dunham, M. M., Evans, II, N. J., Terebey, S., Dullemond, C. P., & Young, C. H. 2010, *ApJ*, 710, 470

Dunham, M. M., Allen, L. E., Evans, II, N. J., et al. 2015, *ApJS*, 220, 11

Eiroa, C., & Casali, M. M. 1992, *A&A*, 262, 468

Enoch, M. L., Evans, II, N. J., Sargent, A. I., & Glenn, J. 2009, *ApJ*, 692, 973

Evans, Neal J., I., Di Francesco, J., Lee, J.-E., et al. 2015, *ApJ*, 814, 22

Evans, II, N. J., Dunham, M. M., Jørgensen, J. K., et al. 2009, *ApJS*, 181, 321

Fischer, W. J., Megeath, S. T., Furlan, E., et al. 2017, *ApJ*, 840, 69

Gutermuth, R. A., Megeath, S. T., Myers, P. C., et al. 2009, *ApJS*, 184, 18

Harsono, D., Bjerkeli, P., van der Wiel, M. H. D., et al. 2018, *Nature Astronomy*, 2, 646

Hartmann, L., Herczeg, G., & Calvet, N. 2016, *ARA&A*, 54, 135

Harvey, P. M., Chapman, N., Lai, S.-P., et al. 2006, *ApJ*, 644, 307

Herbig, G. H. 1977, *ApJ*, 217, 693

—. 2008, *AJ*, 135, 637

Herbst, T. M., Beckwith, S. V. W., & Robberto, M. 1997, *ApJL*, 486, L59

Herczeg, G. J., Johnstone, D., Mairs, S., et al. 2017, *ApJ*, 849, 43

Herczeg, G. J., Kuhn, M. A., Zhou, X., et al. 2019, *ApJ*, 878, 111

Hillenbrand, L. A., & Findeisen, K. P. 2015, *ApJ*, 808, 68

Hodapp, K. W. 1999, *AJ*, 118, 1338

Hodapp, K. W., Chini, R., Watermann, R., & Lemke, R. 2012, *ApJ*, 744, 56

Hsieh, T.-H., & Lai, S.-P. 2013, *ApJS*, 205, 5

Hunter, T. R., Brogan, C. L., MacLeod, G., et al. 2017, *ApJL*, 837, L29

Johnstone, D., Hendricks, B., Herczeg, G. J., & Bruderer, S. 2013, *ApJ*, 765, 133

Johnstone, D., Herczeg, G. J., Mairs, S., et al. 2018, *ApJ*, 854, 31

Jørgensen, J. K., van Dishoeck, E. F., Visser, R., et al. 2009, *A&A*, 507, 861

Jørgensen, J. K., Visser, R., Williams, J. P., & Bergin, E. A. 2015, *A&A*, 579, A23

Jørgensen, J. K., Visser, R., Sakai, N., et al. 2013, *ApJL*, 779, L22

Kenyon, S. J., Hartmann, L. W., Strom, K. M., & Strom, S. E. 1990, *AJ*, 99, 869

Kim, H. J., Evans, II, N. J., Dunham, M. M., Lee, J.-E., & Pontoppidan, K. M. 2012, *ApJ*, 758, 38

Kospal, A., Nemeth, P., Abraham, P., et al. 2008, *Information Bulletin on Variable Stars*, 5819

Lee, J.-E. 2007, *Journal of Korean Astronomical Society*, 40, 83

Lee, J.-E., Bergin, E. A., & Evans, II, N. J. 2004, *ApJ*, 617, 360

Lee, J.-E., Lee, S., Baek, G., et al. 2019, *Nature Astronomy*, arXiv:1809.00353

Lee, K. I., Fernández-López, M., Storm, S., et al. 2014, *ApJ*, 797, 76

Liu, S.-Y., Su, Y.-N., Zinchenko, I., Wang, K.-S., & Wang, Y. 2018, *ApJL*, 863, L12

Lodato, G., & Clarke, C. J. 2004, *MNRAS*, 353, 841

Loinard, L., Zapata, L. A., Rodríguez, L. F., et al. 2013, *MNRAS*, 430, L10

Long, F., Herczeg, G. J., Harsono, D., et al. 2019, *ApJ*, 882, 49

Lorenzetti, D., Antoniucci, S., Giannini, T., et al. 2012, *ApJ*, 749, 188

Mairs, S., Johnstone, D., Kirk, H., et al. 2017, *ApJ*, 849, 107

Masunaga, H., & Inutsuka, S.-i. 2000, *ApJ*, 531, 350

McMullin, J. P., Waters, B., Schiebel, D., Young, W., & Golap, K. 2007, in *Astronomical Society of the Pacific Conference Series*, Vol. 376, *Astronomical Data Analysis Software and Systems XVI*, ed. R. A. Shaw, F. Hill, & D. J. Bell, 127

Min, M., Dullemond, C. P., Kama, M., & Dominik, C. 2011, *Icarus*, 212, 416

Miotello, A., Testi, L., Lodato, G., et al. 2014, *A&A*, 567, A32

Müller, H. S. P., Thorwirth, S., Roth, D. A., & Winnewisser, G. 2001, *A&A*, 370, L49

Natta, A., Testi, L., Calvet, N., et al. 2007, *Protostars and Planets V*, 767

Nayakshin, S., & Lodato, G. 2012, *MNRAS*, 426, 70

Ortiz-León, G. N., Loinard, L., Mioduszewski, A. J., et al. 2015, *ApJ*, 805, 9

Ortiz-León, G. N., Dzib, S. A., Kounkel, M. A., et al. 2017, *ApJ*, 834, 143

Oya, Y., Sakai, N., Sakai, T., et al. 2014, *ApJ*, 795, 152

Oya, Y., Sakai, N., Watanabe, Y., et al. 2017, *ApJ*, 837, 174

Plunkett, A. L., Arce, H. G., Mardones, D., et al. 2015, *Nature*, 527, 70

Reipurth, B., Yu, K. C., Heathcote, S., Bally, J., & Rodríguez, L. F. 2000, *AJ*, 120, 1449

Ricci, L., Testi, L., Natta, A., et al. 2010, *A&A*, 512, A15

Safron, E. J., Fischer, W. J., Megeath, S. T., et al. 2015, *ApJL*, 800, L5

Sakai, N., Sakai, T., Hirota, T., et al. 2014, *Nature*, 507, 78

Shu, F. H. 1977, *ApJ*, 214, 488

Testi, L., Birnstiel, T., Ricci, L., et al. 2014, *Protostars and Planets VI*, 339

Tripathi, A., Andrews, S. M., Birnstiel, T., & Wilner, D. J. 2017, *ApJ*, 845, 44

van 't Hoff, M. L. R., Tobin, J. J., Trapman, L., et al. 2018, *ApJL*, 864, L23

Visser, R., Bergin, E. A., & Jørgensen, J. K. 2015, *A&A*, 577, A102

Vorobyov, E. I., & Basu, S. 2005, *ApJL*, 633, L137

—. 2010, *ApJ*, 719, 1896

Williams, J. P., & Cieza, L. A. 2011, *ARA&A*, 49, 67

Yen, H.-W., Liu, H. B., Gu, P.-G., et al. 2016, *ApJL*, 820, L25

Yen, H.-W., Takakuwa, S., Ohashi, N., et al. 2014, *ApJ*, 793, 1

Yoo, H., Lee, J.-E., Mairs, S., et al. 2017, *ApJ*, 849, 69

Zhu, Z., Hartmann, L., Gammie, C., & McKinney, J. C. 2009, *ApJ*, 701, 620

Table 1. Detected molecular lines

Molecule	Frequency (GHz)	Transition	$\log_{10} A^a$ (s ⁻¹)	E_{up}^b (K)	g_{up}^c
C ¹⁷ O	337.060988 ^d	J= 3–2	-5.63433	32.4	12
C ³⁴ S	337.396459	J= 7–6	-3.11804	50.2	15
CH ₃ OH	338.3446280 ^e	7(-1,7)–6(-1,6)	-3.77817	70.5	15
	338.4086810 ^e	7(0,7)–6(0,6)++	-3.76902	65.0	15
	338.7216300 ^e	7(2,6)–6(2,5)	-3.80441	90.9	15
	338.7229400 ^e	7(-2,6)–6(-2,5)	-3.80441	90.9	15
H ¹³ CO ⁺	346.9983440	J= 4–3	-2.48309	41.6	9
CCH	349.3992756 ^f	N= 4–3, J= 7/2–5/2, F= 4–3	-3.90313	41.9	9
	349.4006712 ^f	N= 4–3, J= 7/2–5/2, F= 3–2	-3.92139	41.9	7
	349.4146425 ^{e,g}	N= 4–3, J= 7/2–5/2, F= 3–3	-5.15397	41.9	7
	349.6036139 ^{e,g}	N= 4–3, J= 7/2–7/2, F= 4–4	-5.28599	41.9	9

NOTE—The molecular information is adopted from CDMS database (Müller et al. 2001).

^aEinstein A-coefficient.

^bEnergy state of the upper level.

^cStatistical weight of the upper level.

^dFrequency of the strongest hyper-fine line in C¹⁷O 3–2.

^eMarginally detected line.

^fStrong CCH line.

^gWeak CCH line.

Table 2. Thin disk model for the Continuum emission

ψ^a		1.0	1.5	2.0
$T_{0.1}^a$	(K)	52	50	49
$\tau_{0.1}^a$		1.1	1.4	1.6
r_{max}^b	('')	0.14	0.13	0.13
T_{med}^c	(K)	53	51	50
M_{disk}^d	(M_{\odot})	0.05	0.10	0.23

^aBest fit parameters in the thin disk models (see Figure 13)

^bThe truncated radius of disk producing the observed continuum flux (139.7 mJy).

^cThe surface area weighted temperature within a disk ($r < r_{\text{max}}$).

^dThe disk mass from the thin disk model with the dust opacity of 3.4 cm² g⁻¹ (Beckwith et al. 1990) and the gas to dust ratio of 100.

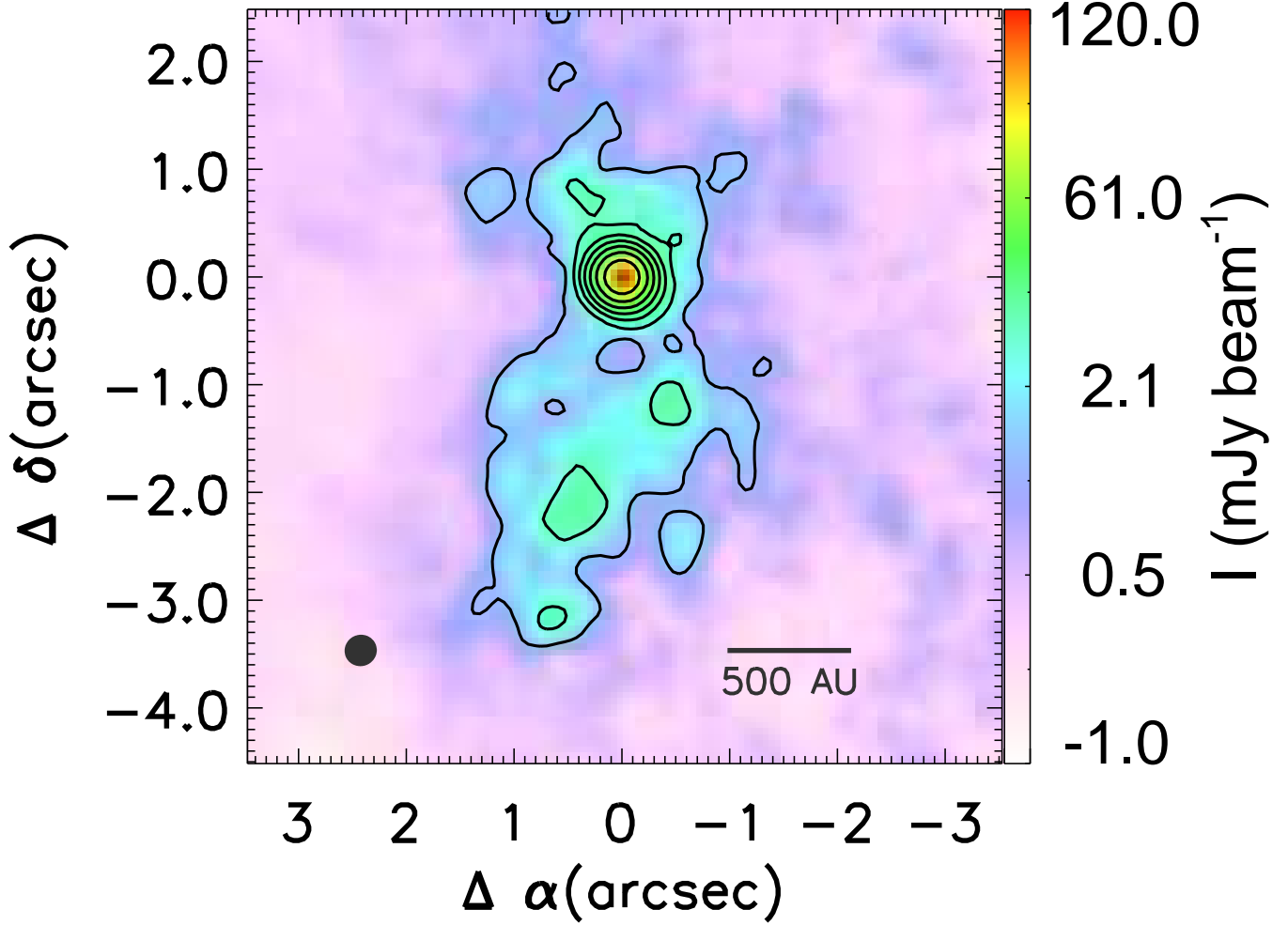


Figure 1. The 873 μm dust continuum image produced with the natural weighting and the UV taper of 0.2''. The contour levels increase by a factor of two from 5σ to 320σ ($1 \sigma = 0.21 \text{ mJy beam}^{-1}$). The origin is the position of the continuum peak for EC 53. The ellipse on the bottom left corner represents the synthesized beam, and the scale bar of 500 AU is presented at the bottom right. Note that the color scale has two linear slopes below and above 2.1 mJy beam^{-1} in order to present the extended emission.

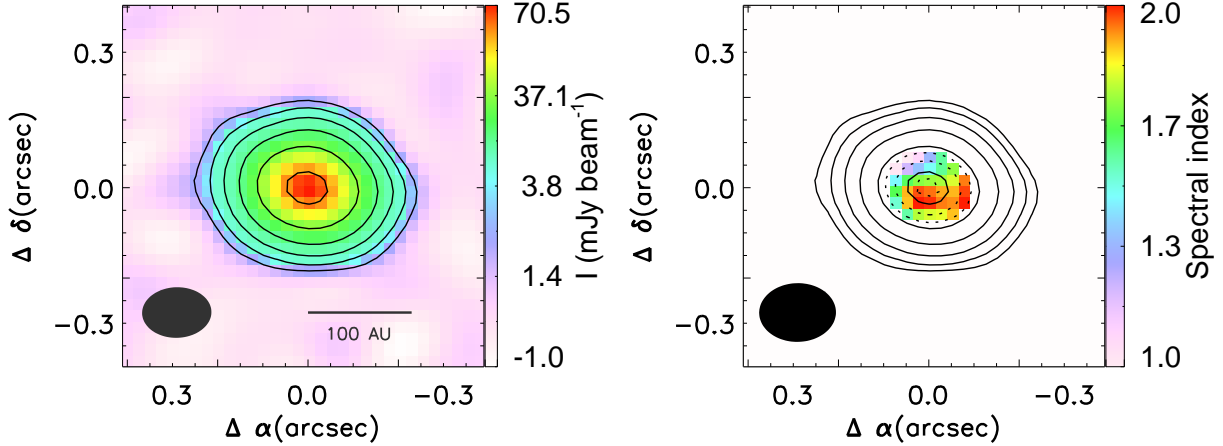


Figure 2. Left: Dust continuum images produced with the uniform weighting. The contour levels increase by a factor of two from 5σ to 160σ ($1\sigma = 0.38\text{ mJy beam}^{-1}$). Note that the color scale has two linear slopes below and above 3.8 mJy beam^{-1} . The black ellipse on the bottom left corner indicates the beam size, and the scale bar of 100 AU is presented at the bottom right. Right: The distribution of the spectral index (α ; $F_\nu \propto \nu^\alpha$) derived from the images produced with the uniform weighting. The solid contours are the same as those on the left panel. The dotted contours represent the 1σ errors of the spectral index from 0.5 (outermost) to 0.3 (innermost) with the step size of 0.1 . The beam size of the image for the spectral index is presented as the black ellipse on the bottom left corner.

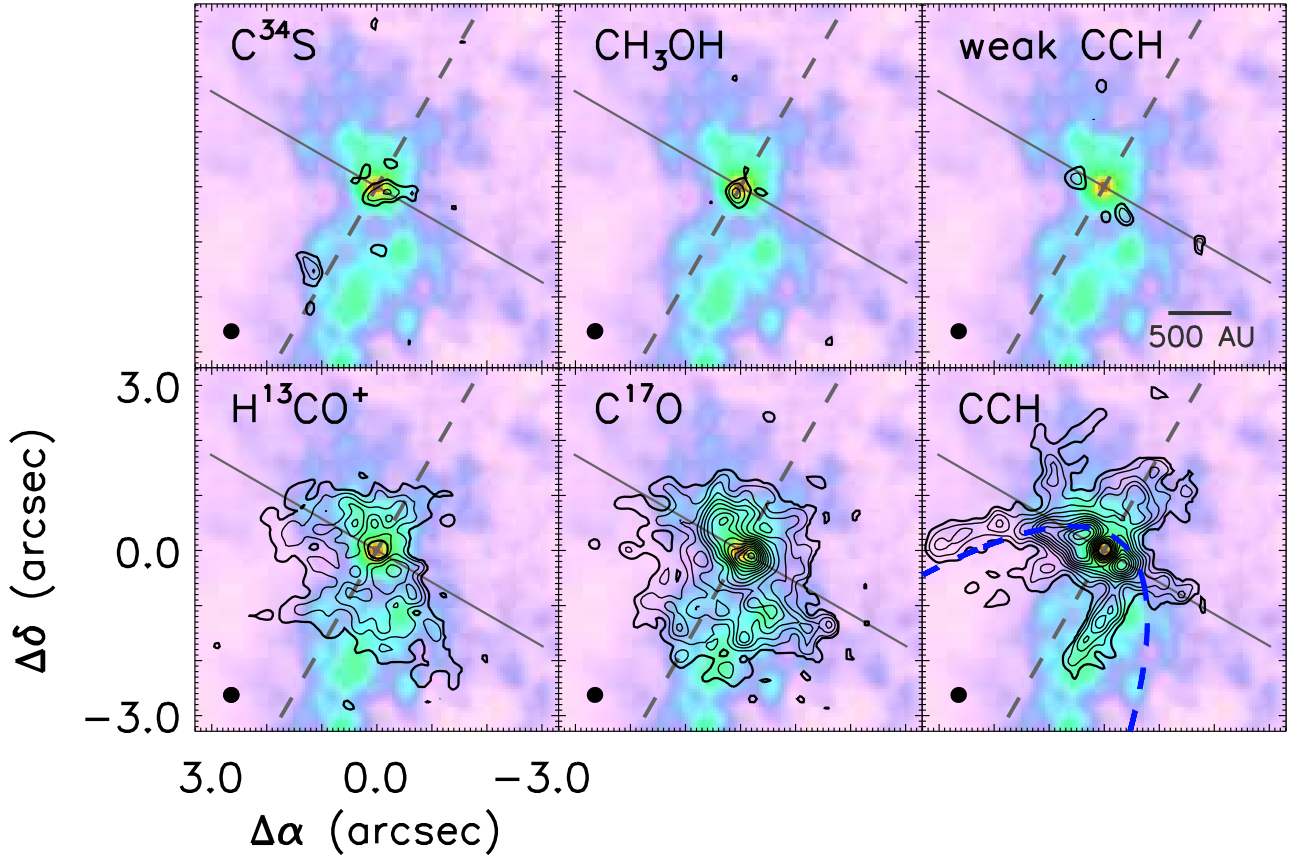


Figure 3. Integrated intensity maps for the detected molecular lines toward EC 53. The background image is the zoom-in of Figure 1. The thick solid and dashed gray lines indicate the disk and outflow directions, respectively. The blue dashed curvature in the bottom right panel indicates the outflow cavity wall traced by a near-IR observation (Hodapp et al. 2012). The ellipses on the bottom left corner represent the synthesized beam. The scale bar of 500 AU is at the bottom right of the weak CCH map. The CH_3OH and weak CCH lines are marginally detected (see Table 1). Those lines of the individual molecules are stacked in order to get a higher signal-to-noise ratio. The 1σ RMS noise, the lowest contour, and subsequent contour step for the individual molecules are as follow: $4.7 \text{ mJy beam}^{-1} \text{ km s}^{-1}$, 3σ , and 1σ for C^{34}S , $2.7 \text{ mJy beam}^{-1} \text{ km s}^{-1}$, 3σ , and 1σ for CH_3OH , $4.4 \text{ mJy beam}^{-1} \text{ km s}^{-1}$, 3σ , and 1σ for weak CCH, $4.6 \text{ mJy beam}^{-1} \text{ km s}^{-1}$, 5σ , and 2σ for H^{13}CO^+ , $4.3 \text{ mJy beam}^{-1} \text{ km s}^{-1}$, 5σ , and 3σ for C^{17}O , $5.6 \text{ mJy beam}^{-1} \text{ km s}^{-1}$, 5σ , and 3σ for CCH.

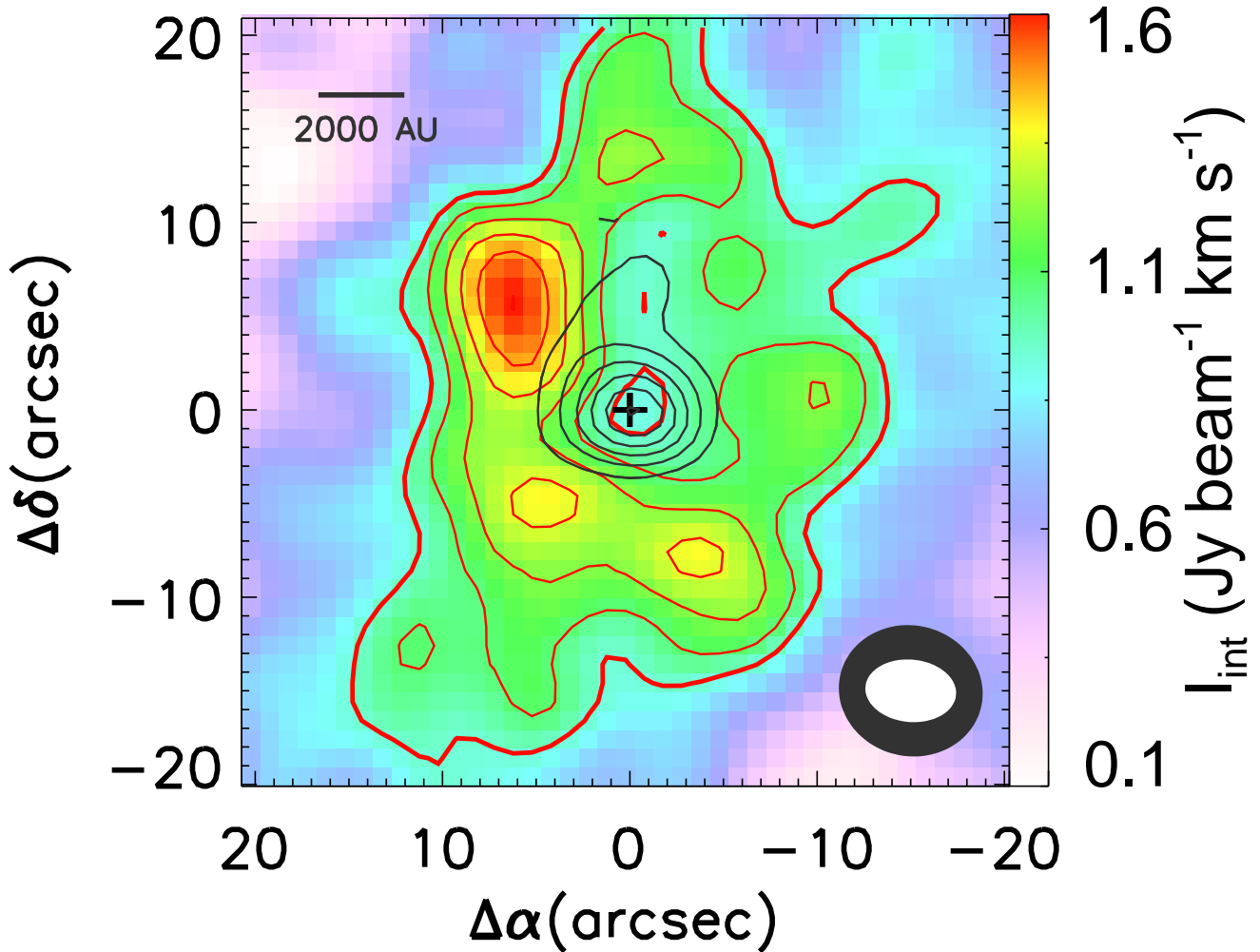


Figure 4. Integrated intensity maps for the hyperfine $F_1 F = 01 - 12$ line of N_2H^+ 1-0 (image and red contour) and the C^{17}O 3-2 (black contour) lines toward EC 53. The N_2H^+ image is extracted from the achieve data observed by CARMA (Lee et al. 2014) and is integrated from -1.5 to $+1.5 \text{ km s}^{-1}$. The lowest level and step of contours are 5 and 1σ ($1\sigma = 0.14 \text{ Jy beam}^{-1} \text{ km s}^{-1}$), respectively. The black contours (10σ , 20σ , 30σ , and 40σ RMS levels, $1\sigma = 132 \text{ mJy beam}^{-1} \text{ km s}^{-1}$) indicate the integrated intensity map of C^{17}O 3-2 line observed with ACA (W. Park et al. in prep.). The beam sizes of CARMA and ACA are presented as the black and white ellipses on the right bottom corner, respectively. The scale bar of 2000 AU is at the top left. The N_2H^+ molecule is depleted around EC 53 where the C^{17}O line emission is detected.

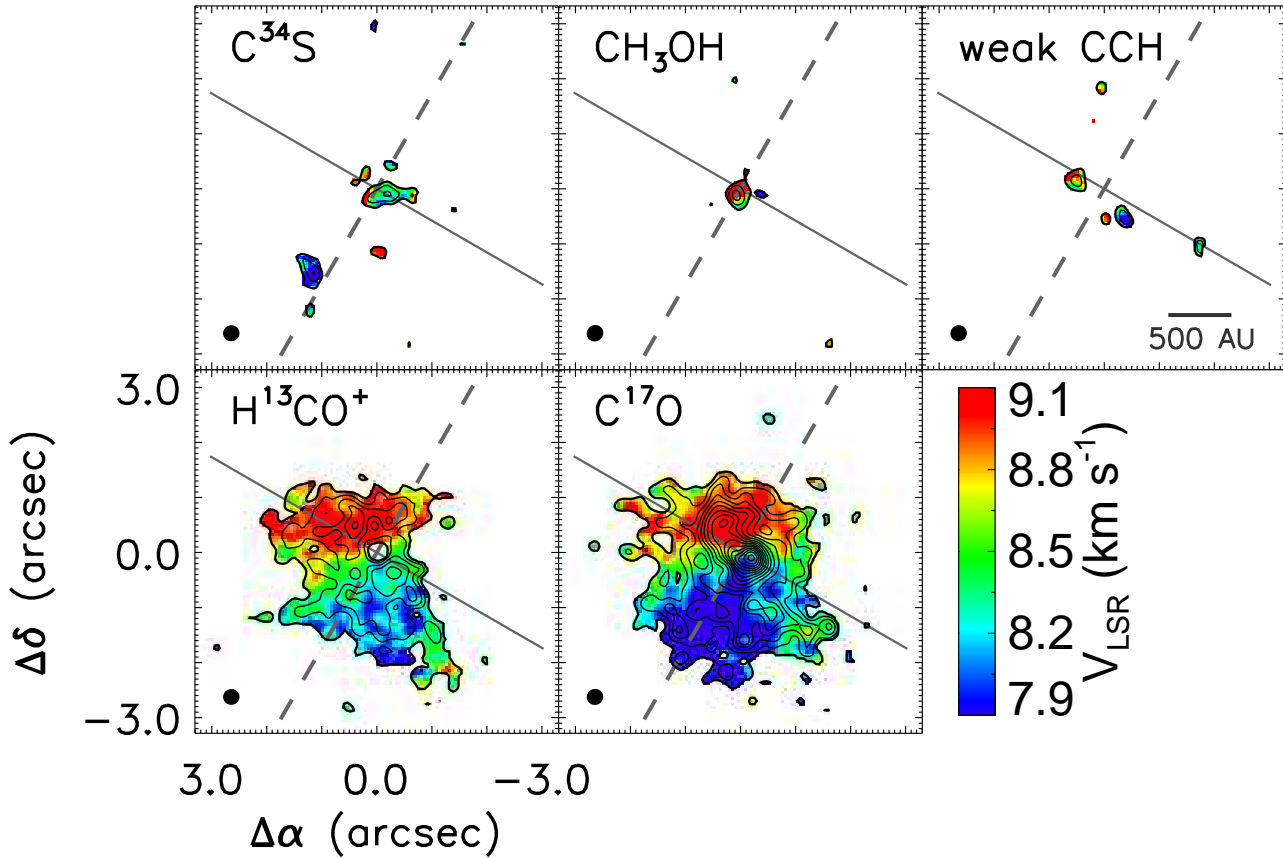


Figure 5. Integrated intensity maps (contours) and intensity weighted velocity maps (images) for the detected molecular lines toward EC 53 except for CCH. The contours are the same as Figure 3.

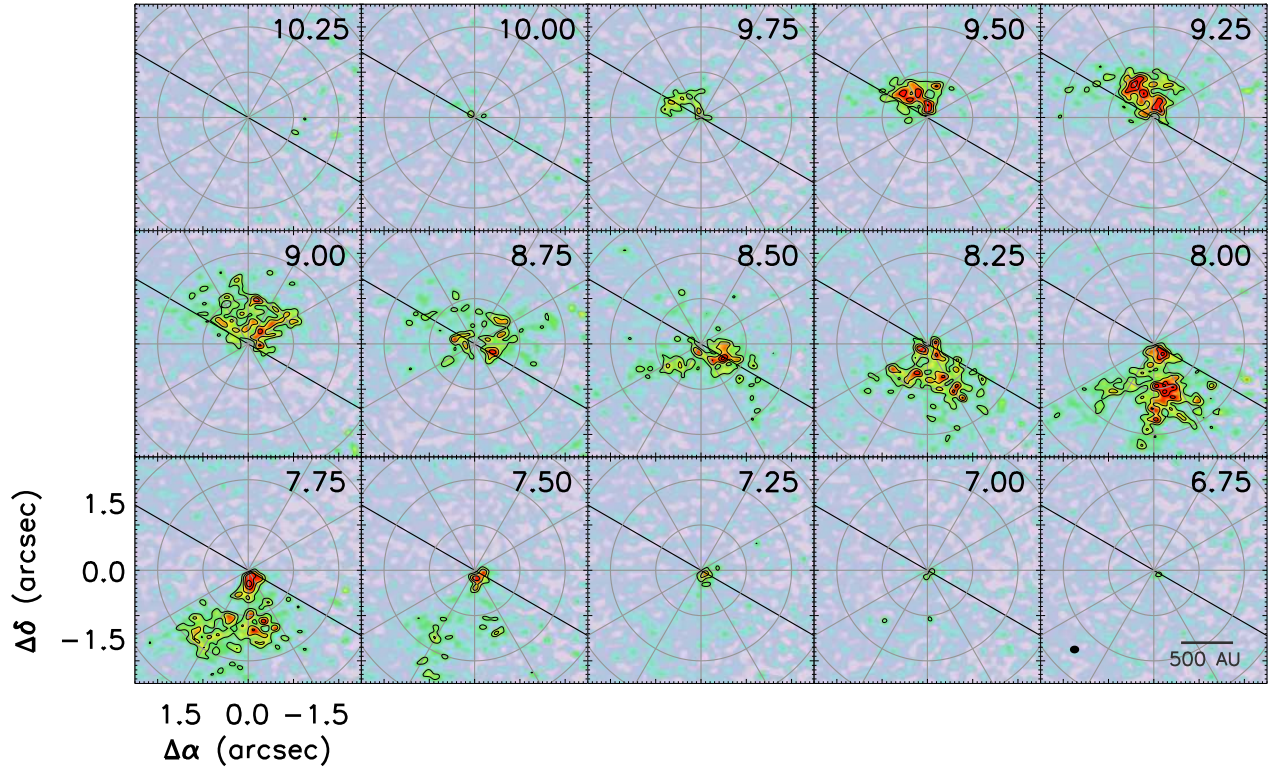


Figure 6. Velocity channel maps of C^{17}O 3–2. The data are extracted from the briggs weighting image. The contour levels start from 4σ and increase in step of 2σ ($1\sigma = 3.85 \text{ mJy beam}^{-1}$). The gray lines and circles are plotted in step of 30° and $1.0''$, respectively, to identify the position of emission clearly. The synthesized beam and the scale bar of 500 AU are presented at the bottom left and right, respectively, in the panel with the velocity of 6.75 km s^{-1} .

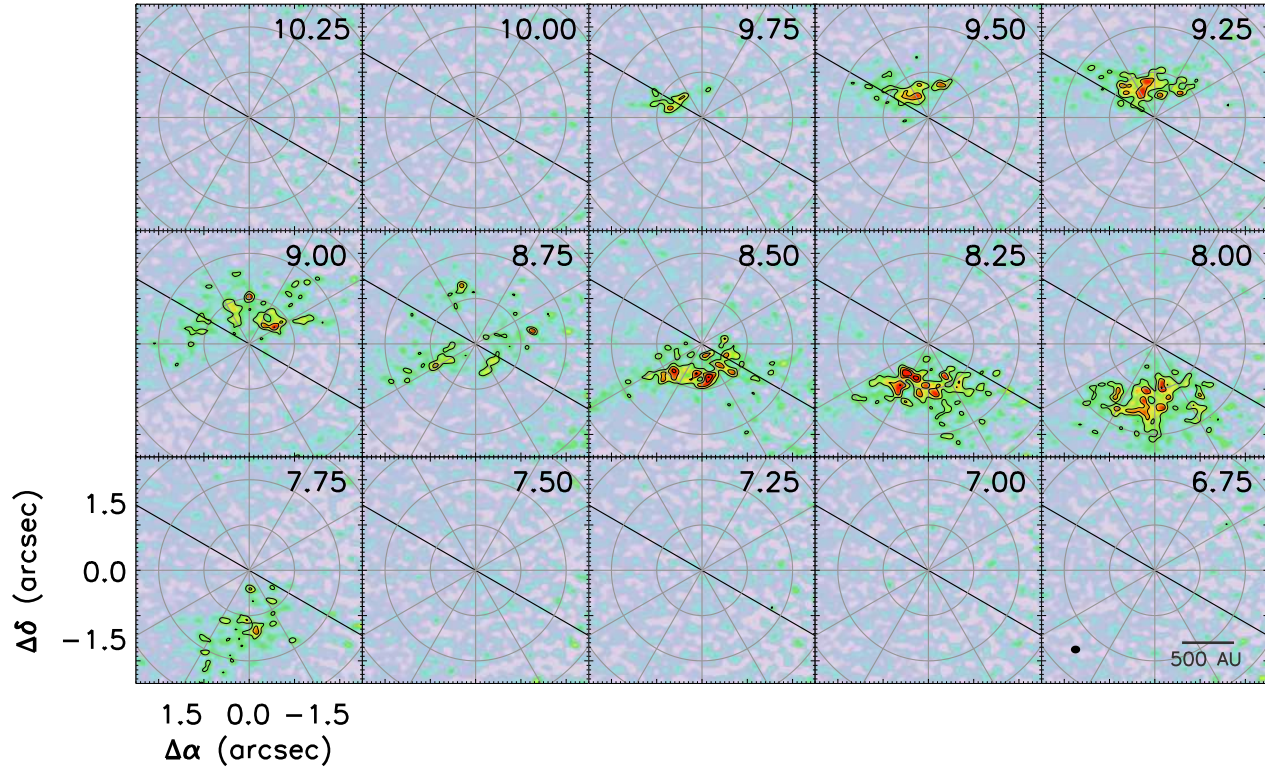


Figure 7. Same as Figure 6 except for H^{13}CO^+ 4–3. The RMS noise level (1σ) is $4.13 \text{ mJy beam}^{-1}$.

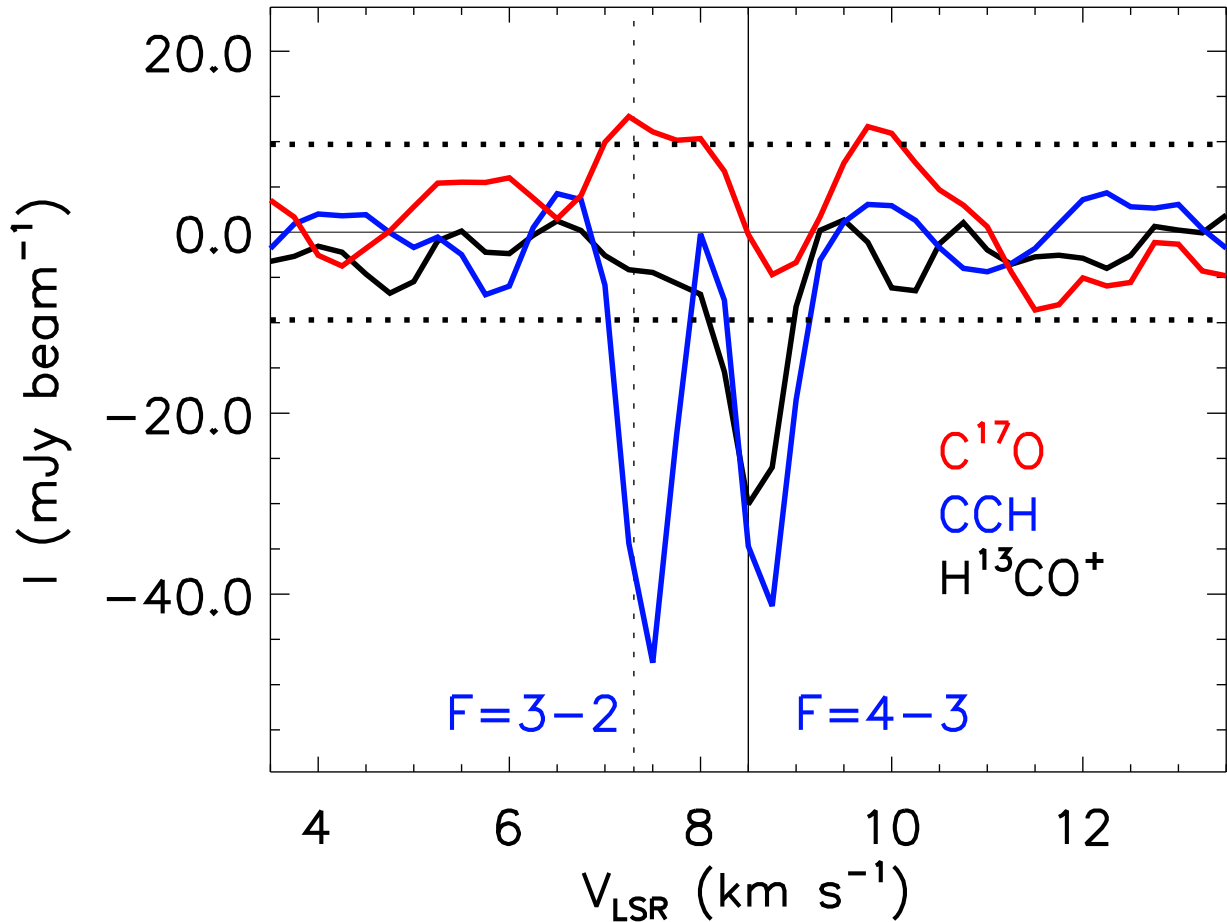


Figure 8. The spectra of H^{13}CO^+ (black), CCH (blue), and C^{17}O (red) at the continuum peak. The spectra are extracted from the briggs weighting images and Hanning-smoothed. The solid vertical black line indicates the source velocity (8.5 km s^{-1}). The dotted vertical line indicates the line center of the CCH $F = 3-2$. The dotted horizontal black lines show $\pm 3 \sigma$ of the C^{17}O ($1\sigma = 3 \text{ mJy beam}^{-1}$).

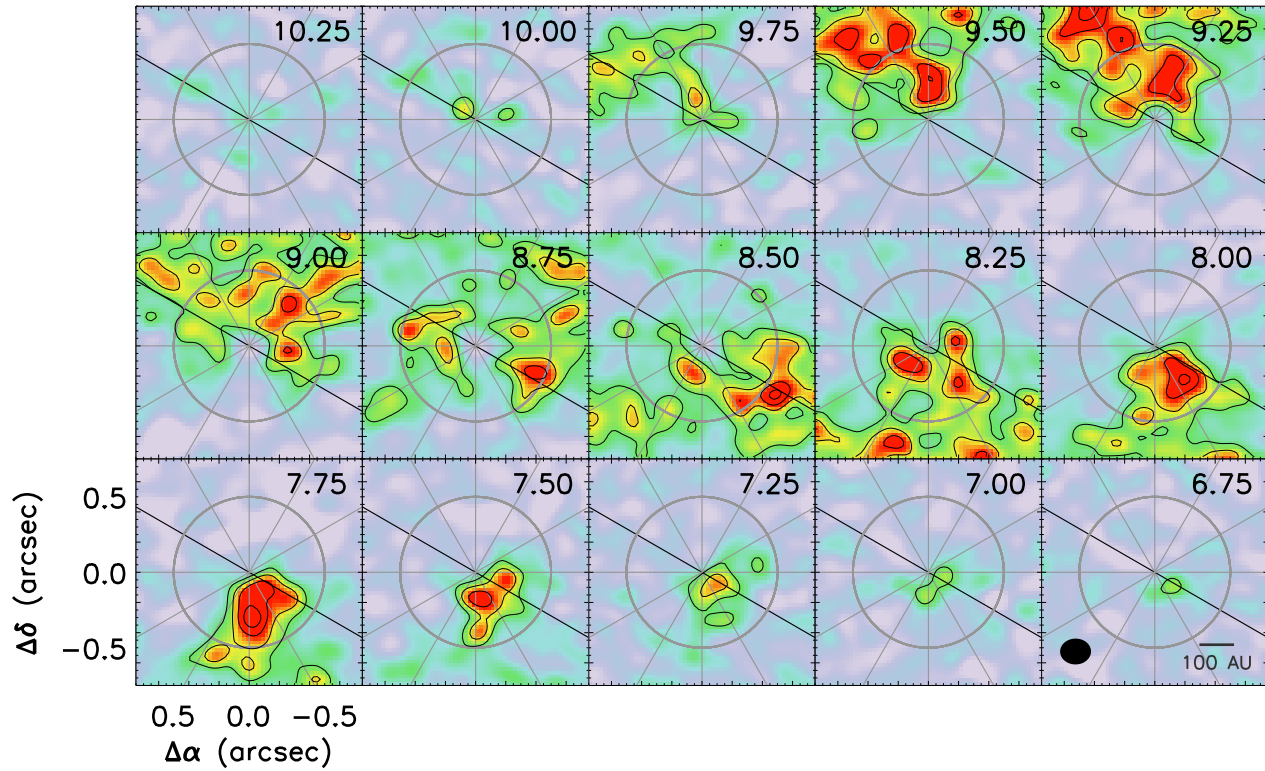


Figure 9. Zoom-in of Figure 6. The gray circle indicates the radius of $0.5''$.

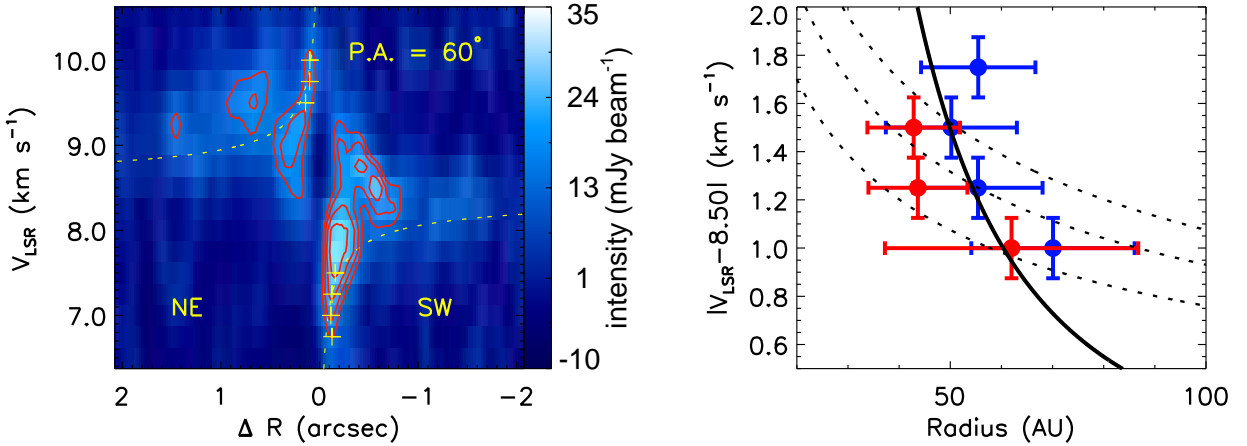


Figure 10. Position-velocity diagram (left) and rotation profile (right) of C^{17}O 3–2 along the disk direction with a position angle of 60° . Left: The image and red contours indicate the observed C^{17}O intensity extracted from the briggs weighting image. The contours start from 4σ in step of 1σ ($1\sigma = 3.8 \text{ mJy beam}^{-1}$). The dashed yellow lines represent the Keplerian motion with a protostellar mass of $0.3 M_\odot$. Right: The red (blue) points indicate the peak positions along given red-shifted (blue-shifted) velocity channels as shown in the yellow cross in the left panel. Three dotted lines represent the Keplerian motion with a protostellar mass of 0.4 (top), 0.3 (middle), and $0.2 M_\odot$ (bottom), respectively. When these data are fit with a power-law function, the power law index is -2.1 ± 2.2 (black solid line).

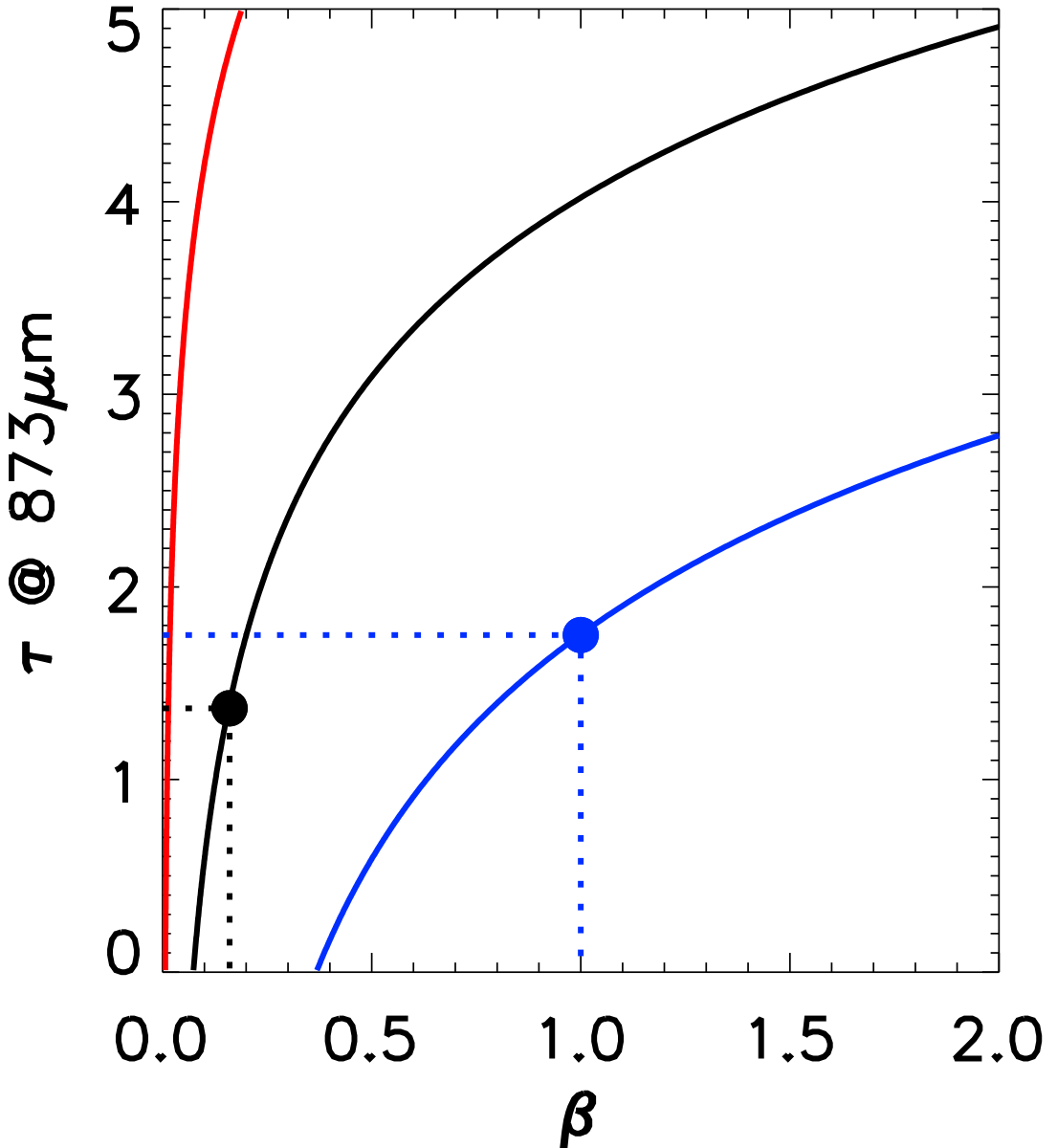


Figure 11. The optical depth at $873 \mu\text{m}$ (τ) and the power-law index of dust opacity (β) producing the spectral index (α) of 1.9 for the given dust temperatures: 20 (blue), 50 (black), and 80 K (red), respectively. The blue circle indicates the τ producing $\alpha=1.9$ for the temperature of 20 K and $\beta=1$ used to calculate the disk mass (Section 3.1) while the black circle indicates the β producing $\alpha=1.9$ for the temperature of 50 K and $\tau=1.4$ derived from the thin disk model (see Table 2).

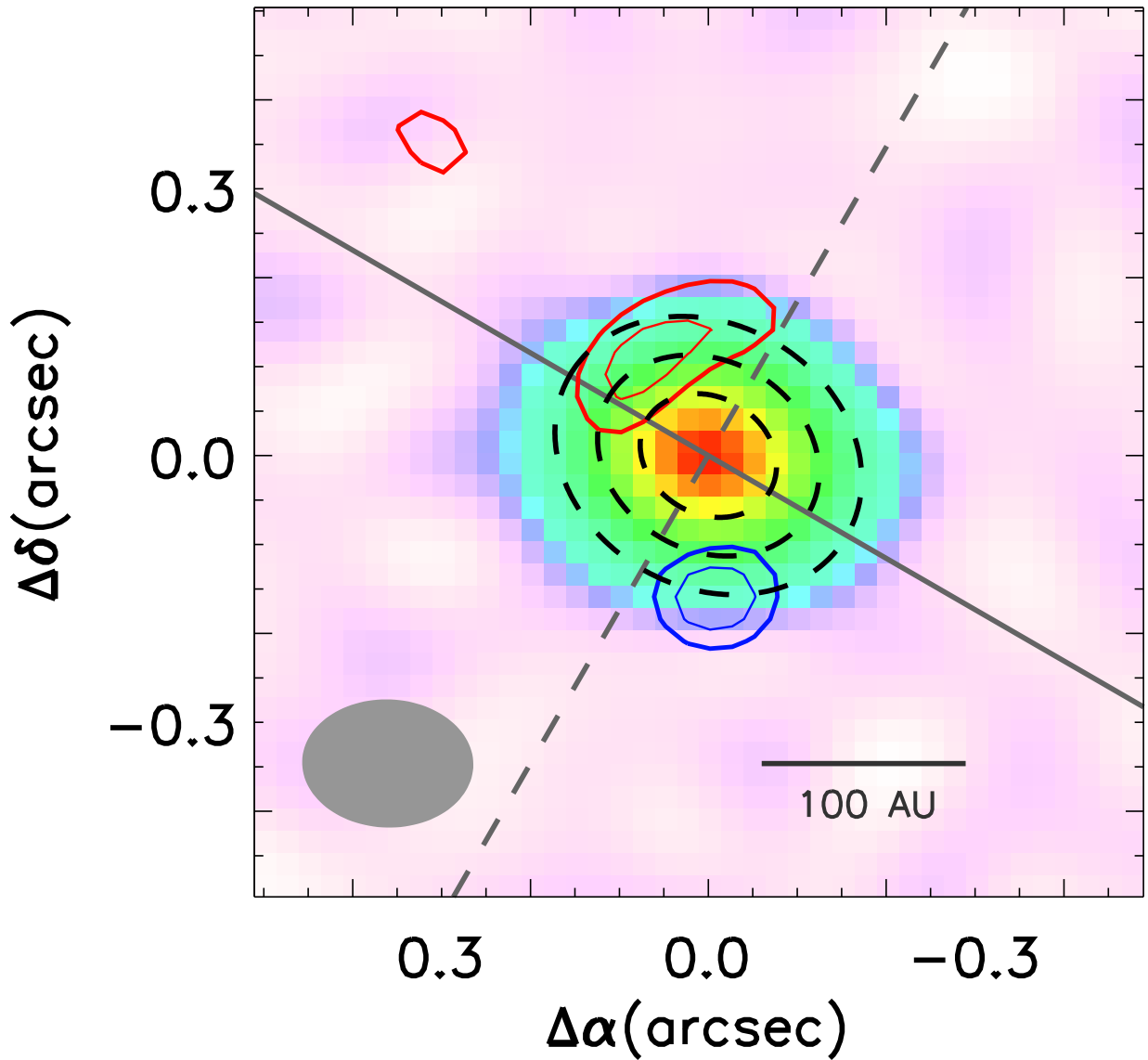


Figure 12. The C^{17}O 3–2 integrated intensity map (contour) of EC 53 produced by the uniform weighting. The red and blue contours indicate the red- and blue-shifted components, respectively, integrated over the velocity from 1.0 to 1.5 km s^{-1} with respect to the source velocity. The lowest contour and subsequent contour step are 5σ and 1σ , respectively ($1\sigma = 3.5 \text{ mJy beam}^{-1} \text{ km s}^{-1}$). The background image is the dust continuum intensity as in the left panel of Figure 2. Three dashed ellipses correspond to the radii of 0.08, 0.13, and $0.18''$, respectively. The beam size and 100 AU scale bar are shown in the bottom left and right corners, respectively.

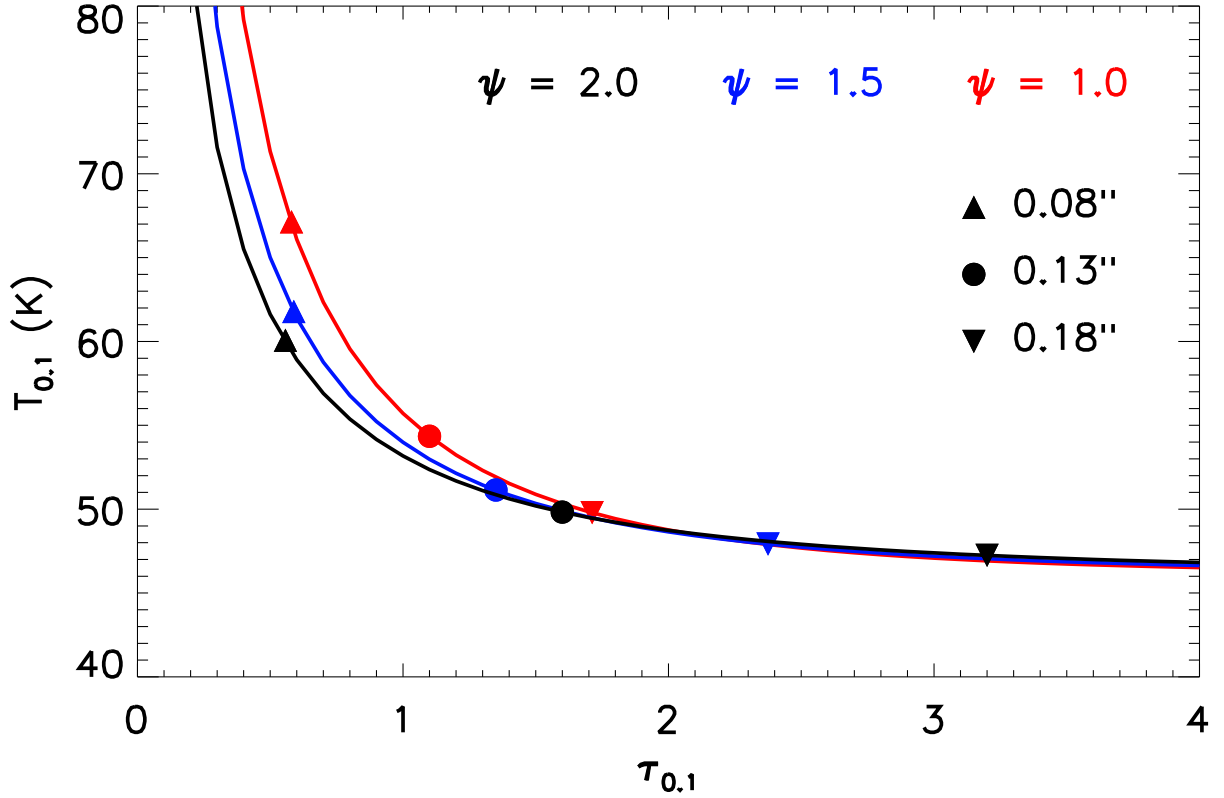


Figure 13. Model parameters producing the C^{17}O emission distribution shown in Figure 12. The lines indicate the continuum optical depth ($\tau_{0.1}$) and the dust temperature ($T_{0.1}$) at $0.1''$ which reproduce the continuum intensity ($69.3 \pm 0.4 \text{ mJy beam}^{-1}$) at the continuum peak. Different colors indicate different power-law indices of optical depth (see Equation (4)). The upward triangles, circles, and downward triangles indicate the model parameters producing the C^{17}O emission peak at $0.08''$, $0.13''$, and $0.18''$, respectively, which are marked by the dashed ellipses in Figure 12.

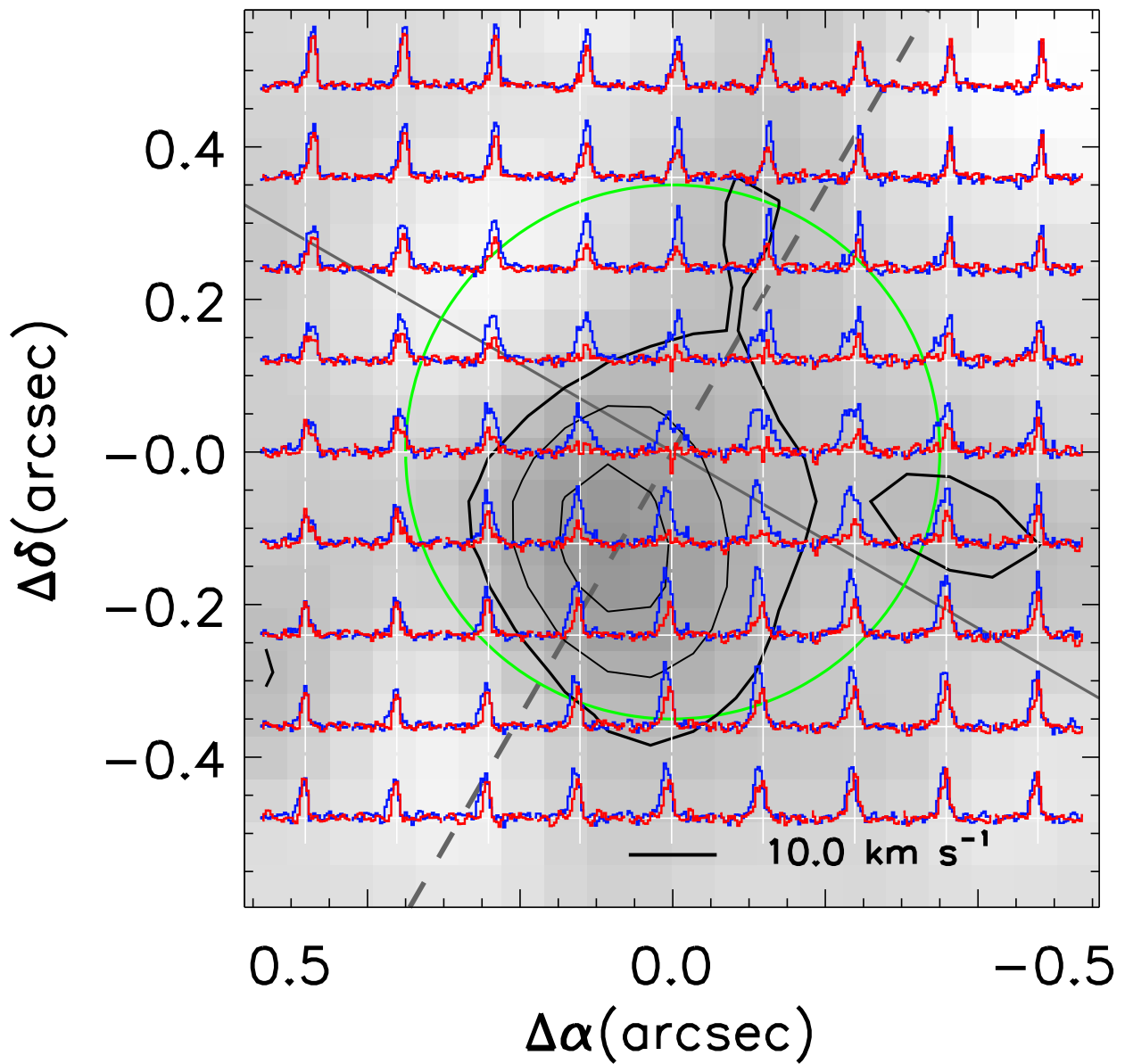


Figure 14. The spectral maps of C^{17}O (blue) and H^{13}CO^+ (red) on top of the CH_3OH integrated intensity map (image and contour). The contour levels are the same as those in Figure 5. The horizontal bar on the bottom indicates the scale of the x-axis (velocity range from -5 to 5 km s^{-1}). The horizontal and vertical white lines indicate the continuum level and the source velocity, respectively. The green circle indicates the radius of $0.35''$ (153 AU at the distance of 436 pc).

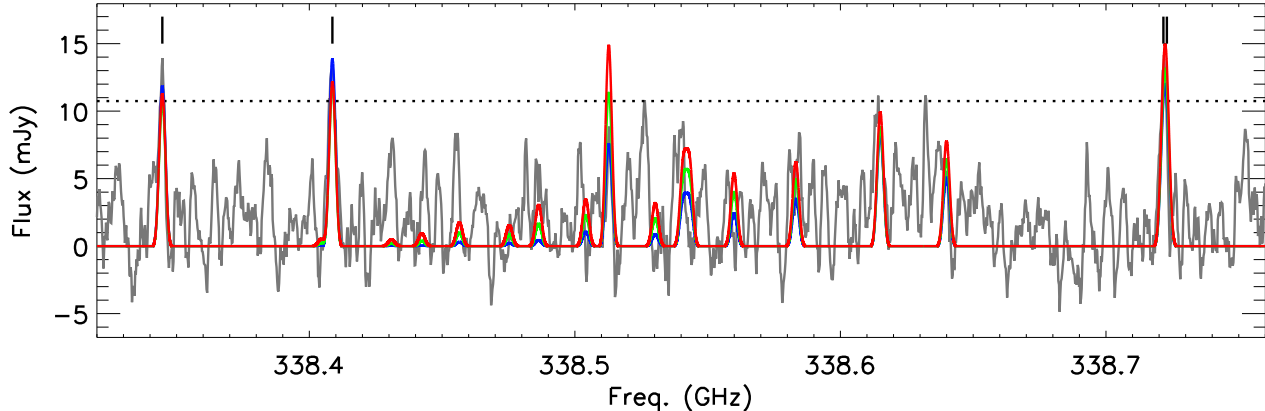


Figure 15. The methanol spectra for EC 53. The gray line shows the observed spectra extracted with the aperture of $0.6''$. The spectra are smoothed with the boxcar of 1.8 km s^{-1} . The black dotted line indicates the 5σ level ($1\sigma = 2.1 \text{ mJy}$). The four vertical black bars indicate the marginally detected CH_3OH lines presented in Table 1. The red, green, and blue lines show the model spectra with the temperatures of 70, 50, and 30 K and with the methanol column densities of 5.2 , 3.7 , and $2.2 \times 10^{15} \text{ cm}^{-2}$, respectively.